Fabrication and experimental demonstration of a hybrid resonant acoustic gradient index metasurface at 40kHz

Nikhil JRK Gerard,[1] Huachen Cui,[2] Chen Shen,[3] Yangbo Xiey,[3] Steven Cummer,[3] Xiaoyu Zheng,[2, a)] and Yun Jing[1, b)]

[1)] *Department of Mechanical and Aerospace Engineering, North Carolina State University, Raleigh, North Carolina 27695, USA*

[2)] *Department of Mechanical Engineering, Virginia Tech, Blacksburg, VA 24060, USA*

[3)] *Department of Electrical and Computer Engineering, Duke University, Durham, North Carolina 27708, USA*

(Dated: 4 March 2019)

Over the past few years, gradient index metasurfaces(GIMs) have been voraciously studied for numerous wave control capabilities that they facilitate. In this regard, a hybrid structure consisting of shunted Helmholtz resonators and a straight channel is often chosen as building blocks of the metasurfaces. Prior research, however, has primarily focused on GIMs that operate in audible frequency range, due to the difficulties in fabricating such intricate structures at the millimeter and sub-millimeter scales, for ultrasonic applications. In this paper, we design, fabricate and experimentally realize a GIM for airborne ultrasound at 40kHz. The fabrication of such a GIM is made possible by projection micro-stereolithography, an emerging additive manufacturing technique capable of micro-scale, high aspect-ratio features over a wide area. Numerical simulations were first conducted to verify the metasurface design. Experiments were subsequently performed to corroborate the simulations and the theory. The thermoviscous effects associated with ultrasonic frequencies, their potential applications as well as optimal design strategies for minimal dissipations are discussed.

The emergence of metasurfaces[1–8] has bolstered interests of various engineering communities in compact wave-based devices. Several studies over the past decade have thus proposed sub-wavelength structures that facilitate passive wavefront manipulation[9–12]. In acoustics, not only has this unfolded the realization of novel designs[13–15], but also has revisited classical structures that could now be redesigned to provide unusual functionalities[4,11,12]. Inspired by the diverse features that could be further explored, recent works in this area have revolved around employing such structures to contemporary design strategies. In this context, GIMs have been ardently examined to propose several features such as focusing[14], bending[11], retro-reflection[16,17], and holographic rendering[18]. Additionally, some recent works have examined and embraced the inherent dissipation[19–21] in these GIMs, as not just a loss but an avenue to more unconventional applications such as asymmetric transmission[7,22] and wide-angle absorption[23]. A hybrid design consisting of shunted Helmholtz resonators and a straight channel is a frequent candidate for the building blocks of these structures, due to their relative simplicity and high sound transmission. The fabrication of such structures has been enabled by conventional 3D printing techniques such as fused deposition modeling[?] or stereo-lithography[24,25]. The precision of these manufacturing methods, however, has rendered its implementation in the ultrasound range rather scarce[6,26]. Metasurface-based designs operating at ultrasound frequencies would be advantageous for a variety of applications such as levitation[6,27], sensing, and imaging[28], owing to the better precision brought about by the smaller wavelengths.

Ongoing developments in the field of mechanical metamaterials is accompanied by the ~~rapid evolution~~~~(Z: advances)~~ of manufacturing approaches that help put forward artificial materials with exceptional mechanical properties. Such materials possess complex three dimensional micro- and nano-architectures and hence require sophisticated manufacturing capabilities. Projection micro-stereolightography(PμSL)[29,30], in this regard, is an emerging additive manufacturing technique that is capable of fabricating samples with high structural complexity and feature size ranging from a few micrometers to tens of centimeters - a characteristic that could benefit the fabrication of acoustic metasurfaces/metamaterials at ultrasound frequencies.

In this work, we design, fabricate and experimentally demonstrate the performance of a hybrid resonant acoustic gradient index metasurface (HRAGIM), that operates at 40 kHz. The fabrication of the designed prototype is made possible by the aforementioned additive manufacturing technique. The role of thermoviscous dissipation in its elementary units is discussed and full wave simulations that incorporate these losses are put forward. The results from these simulations are then validated via experimental measurements ~~that are~~ obtained from a two-dimensional experimental platform. The challenges at ultrasound frequencies such as stronger dissipation are highlighted.

The HRAGIM has elementary units which consist of a series of four sub-wavelength Helmholtz resonators(HRs) and an open channel. While the shunted resonators provide the reactance to shift the phase of the incident wave, the open channels serve as sub-wavelength slits that enhance the rate of transmission due to Fabry-Pérot resonance. By varying the parameter h_1, shown in Fig 1(a), a full range of phase shifts from 0 to 2π, can be obtained. Numerical simulations were first performed using the pressure acoustics module on COM-

[a)] Electronic mail: raynexcheng@vt.edu
[b)] Electronic mail: yjing2@ncsu.edu

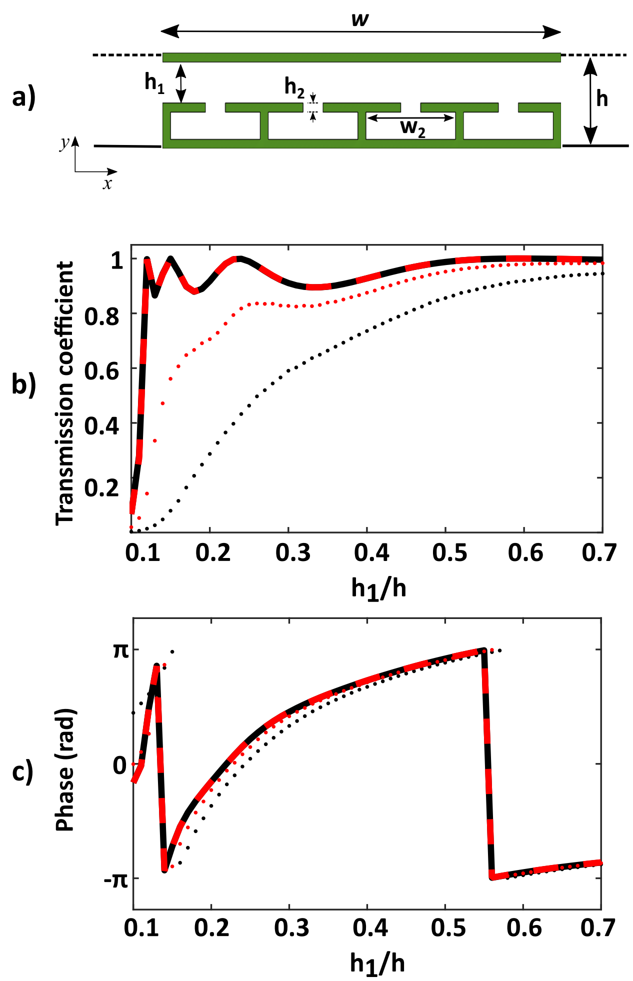

FIG. 1. (a) The elementary unit of the hybrid resonant GIM. To operate at 40 kHz, the dimensions of the unit are: w = 3.428mm, h = 0.857mm, w_2 = 0.9875mm, h_2 = 0.0857mm. The values of h_1 are chosen to be 0.130264mm, 0.152546mm, 0.187683mm, 0.232247mm, 0.318804mm, 0.47635mm to achieve a discretized phase distribution. Numerical prediction of the transmission coefficient (b) and phase shift (c) through the unit cell as a function of h_1/h. The solid black lines and dashed red lines indicates the result at 40 kHz and 3.4 kHz, respectively, for the case without dissipation. Similarly the black and red dots are the results shown when thermoviscous dissipation is included.

SOL Multiphysics 5.3a, a commercial finite element package. The unit cell has fixed height, $h = 0.1\lambda$ and width $w = 0.4\lambda$, where λ is the wavelength of the incident wave. This was done in order to obtain values of h_1, whose phase shifts(ϕ) are equally spaced. As will be discussed later, the material used for fabrication was a high stiffness UV curable acrylate polymer and it is thus safe to assume that the walls of the resonators are acoustically hard, since their impedance is much greater than that of air (Speed of sound, $c \propto \sqrt{E}$, Young's Modulus). The phase gradient, ξ, is then engineered, by arranging the appropriate unit cells in the required pattern where,

$$\xi = \frac{d\phi_s}{dx} = (sin\theta_t - sin\theta_i)k_0, \quad (1)$$

here θ_t is the angle of transmission, θ_i is the angle of incidence and k_0 is the wavenumber. In this case, $\xi = 97.2\ (2\pi{\cdot}\text{rad}{\cdot}\text{m}^{-1})$, where the array period, γ, of the metasurface is 10.284mm. It should be noted that such a GIM for airborne ultrasound can also be formed utilizing other types of unit cells. In this paper, however, we employ the above-mentioned design due to the versatility of the associated hybrid resonances and the firm theoretical framework that prior research in such structures has offered. Here, it is worthwhile mentioning that it is due to this reason that such a design can be scaled as a function of frequency: the GIM in this paper, is an adaptation from the works of Li et al[7,11,12]. The solid black lines and the dashed red lines in Figs. 1(b) and (c) are from pressure acoustics simulations for unit cell designs that operate at 40 kHz and 3430 Hz respectively. This illustrates that the dimensions of the structure that was previously designed to operate at a lower frequency, can be scaled down to work for airborne ultrasound. However, it is pivotal to examine the prospective challenges that such a metasurface could face while operating at higher frequencies. Foremost, as discussed in prior literature,[20,21] the prominent dissipation in such structures is due to the influence of wall friction, owing to the thermoviscous dissipation. This is characterized by, $\Delta = h_1/\delta$, where, h_1, is the slit's transverse dimension (as seen in Fig.1(a)) and $\delta = \sqrt{2\nu/\omega}$, the viscous boundary layer thickness. Here $\nu = 1.45x10^{-5}m^2/s$, is the kinematic viscosity of air, ω is the angular frequency and it is apparent that $\Delta \propto \sqrt{\omega}$. Hence, the largest value of Δ at 3430 Hz, is only 3.67%, while it is 12.53%, for the same value of h_1/h(scaled). This was further examined by performing numerical simulations that solve the thermoviscous acoustics equations in the unit cell region and pressure acoustics equations in the incident and transmitted regions. No-slip and isothermal conditions were imposed on the solid boundaries to incorporate dissipation. The dotted black and red lines, compare the results from these calculations to those carried out on the hybrid resonant structure designed to operate at 3430Hz. It can be seen, that with the incorporation of themoviscous effects, the decrease in transmission coefficient is as expected, much larger in the case of the 40 kHz design than in that of 3430 Hz, as seen in Fig. 1(b). The low rate of transmission for smaller values of h_1/h is also as anticipated, as $\Delta \propto 1/h_1$. In addition to the boundary layer effects, the attenuation of sound, α_s, in free space due the thermal and viscous losses in air, is directly proportional to the square of the frequency, f^2. In the audible range, this attenuation is rather negligible and can be ignored. The higher frequencies however, it becomes more important to take this attenuation into account. In our case, at 40 kHz, $\alpha_s \approx 0.2$Np/m and it's incorporation in our simulations(both unit cell and the upcoming full wave), was still found to have a negligible effect. This may not be the case for frequencies higher than 40 kHz. It is hence important to note that although hybrid resonant GIMs can be scaled as a function of frequency, the effect of losses(Δ and α_s) are more profound at higher frequencies, are not directly scalable. Furthermore, Fig. 1(c) indicates thermoviscous dissipation has a relatively weak influence on phase shift at both 3.4 kHz and 40 kHz. This is true as dissipation dominates the resistance part of impedance

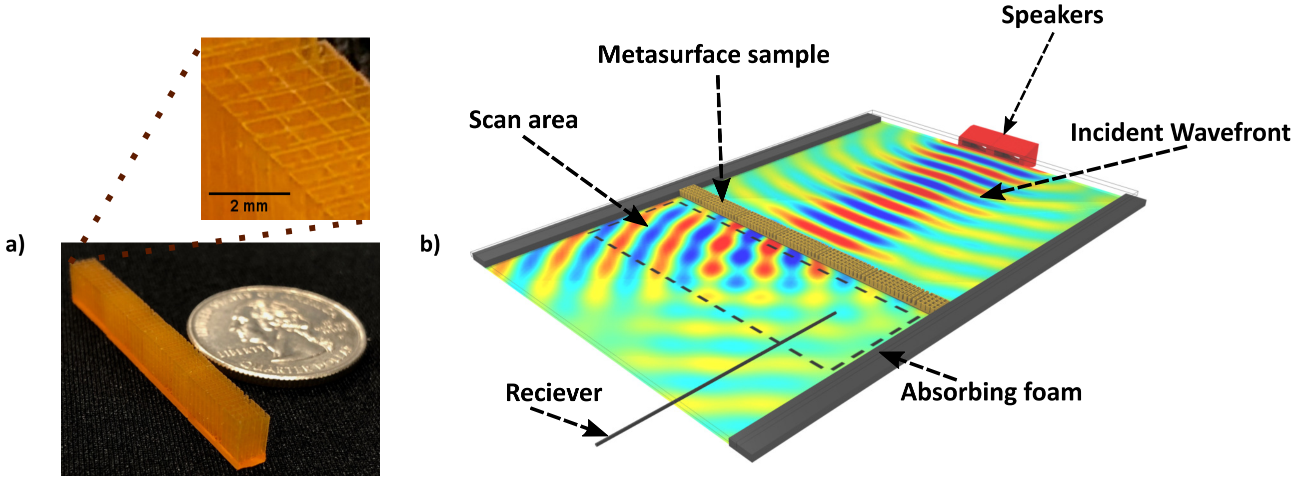

FIG. 2. (a) ~~A~~ sample with thickness 3.428mm and length 61.704mm. The inset shows the zoom of the sample, where the shunted Helmholtz resonators and straight channels can be seen.(b) The scaled down experimental set up of the two-dimensional linear scan stage. Two ultrasonic speakers are connected to tapered horn-type wave guide adapters, that are shown on the right(red), to ensure the incident wavefront. The tube is represented by the black line on the left, which maps the scan area and guides the sound to a receiver.

more than the reactance. The GIM can thus provide the desired wave bending effect for airborne ultrasound, however with a considerable decrease in transmission.

The fabrication of such a minute design is made possible by a high resolution, large area projection microstereolithography system capable of fabricating micro-scale, high-aspect ratio features over a wide area. In contrast to other methods such as fused deposition modeling and UV projection waveguide system, this approach is ideal for samples with high structural complexity and with a feature size ranging from microns to centimeters. A three-dimensional CAD model is first made of the metasurface, which is then sliced into 2D patterns. These patterns are projected via a UV digital micro-mirror device(DMD), focused onto the surface of a photosensitive monomer, which cures under UV exposure. The cured layer in the shape of the 2D slice pattern is then lowered to resupply liquid resin on its surface. The pattern projection is repeated to form the subsequent layer. ~~To improve the resolution of the as-printed metasurfaces, a reduction lens is embedded in the UV light path.~~ To expand the scalability of the printed metasurface, the projection system moves with an optical scanning system to project pattern on multiple areas of the liquid surface, producing large scale metasurfaces with micro-scale resolution. ~~Z: High printing resolution is achieved by embedding a series of reduction lenses along the UV light path.~~

The sample has a width of 3.428mm, is made up of 6 periods and is thus 61.124mm in length, as seen in Fig. 2(a). The material used for fabrication was a custom formulated UV-cured 1,6 – Hexanediol diacrylate polymer, with a low dosage of photo-absorber~~(add the full name of Sudan),~~ which has a young's modulus, E of 512 MPa and Density, 1.1 g/cm^3. The working of this minuscule prototype is then experimentally validated in a 2D waveguide of height 6mm, to ensure that only the fundamental mode can propagate inside (this is hence, also the depth of the third dimension of the sample as seen in Fig. 2(a)). The waveguide shown in Fig. 2(b), is made with laser-cut acrylic plates to confine the transmitted ultrasonic wave in a quasi-two-dimensional space. The entire experimental setup is essentially a scaled-down version of the scan stage used for audible sound in previous works[7–9,31]. It would thus be ideal to use a speaker array to generate a plane wave with a Gaussian amplitude profile to impinge on the metasurface. However, for the convenience of the scaled down measurement platform, the source and the receiver are modified to increase the signal-to-noise ratio associated with the low operating wavelength. Full wave pressure acoustic simulations were performed to help determine the suitable experimental set up. Two single frequency (40 kHz) Murata speakers (MA40S4S) were employed as the source – fitted with tapered horn-type waveguide adapters, which were 3D printed for this purpose. As can be seen in the simulation of this set up on Fig. 2(b), these adapters ensure a planar wavefront to be incident on the metasurface of engineered phase gradient. Perfectly matched layers (PML) were used in the simulations to minimize reflections from the boundaries, which were imitated in experiments by using absorbing foam on both top and bottom. A two-dimensional linear scan stage was programmed to map the field on the transmissive side of the metasurface. This is done by translating a glass tube of diameter 1mm over a rectangular region, with a step size of 2mm. It should be noted that the scattering due to the tube, is negligible as it is much smaller than the wavelength of the propagating sound. At every step, the glass tube guides the sound to a microphone (Murata MA40S4R). An LM358-based operational amplifier was used as the pre-amplification system, from where the signal is transmitted to an NI PCI-6251 data-acquisition board. The collected time-domain signals were then Fourier transformed to the frequency domain to generate the complex field pattern at 40 kHz. Figure 3, shows the results from the measurement in comparison to two sets of full wave simulations - with and without dissipation. The 'without dissipation' case in Fig. 3(A) reaffirms the scalabil-

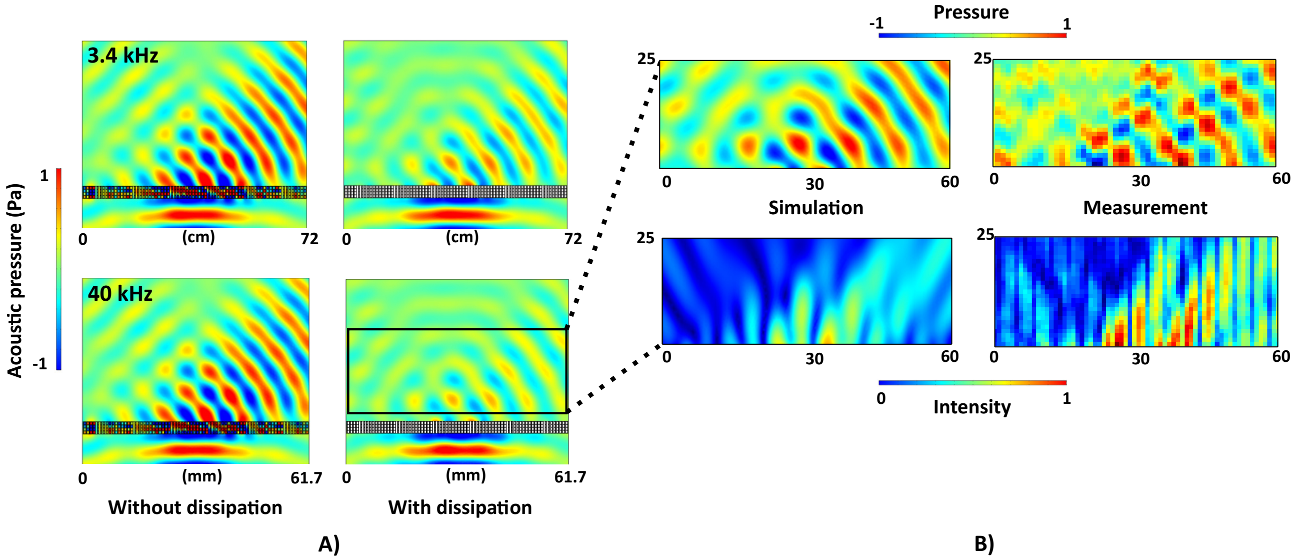

FIG. 3. (a) Simulated acoustic fields that show wavefront bending at both 3.4 kHz (top) and 40 kHz (bottom), for cases with (right) and without (left) dissipation. (b) Comparison of the normalized acoustic pressure and intensity fields for the "with dissipation" case and measured results.

ity of the GIM: Similar wavefront bending is seen for both the 3.4 kHz(top) and 40 kHz(bottom). However, when the thermoviscous effects are incorporated, the effect of loss is more significant in the case of 40 kHz, as discussed previously. The normalized wave field in the 'with dissipation' case in Fig 3(A), is then compared with our measurement results shown in Fig 3(B). A reasonable agreement is seen in the numerical and experimental results, for both complex pressure and intensity. Minor deviations can be attributed to experimental factors such as acoustic structure interaction, that are not taken into account in our numerical simulations. Additionally, the surface roughness/waviness of the sample and the stiffness of the polymer used for fabrication can be further optimized for more precise phase modulation.

In conclusion, we have designed, fabricated and experimentally characterized a minuscule gradient index metasurface that operates at 40 kHz. The scalability of such a design is demonstrated and the role of thermoviscous interactions are discussed. It is clearly seen that dissipation has a greater effect on transmission at higher frequencies. However, its effect on phase is rather negligible and wavefront modulation can therefore be realized. Although the presence of thermoviscous dissipation can act as a limitation for transmissive applications such as bending and focusing, it can be fruitful to engineer compact devices (Z: for) with features such as tunable asymmetric transmission[7,22] and sound absorption[23]. In addition, the diffractive acoustics and the role of multiple internal reflections in the presence of dissipation in such a GIM can be further explored for airborne ultrasound. It is hoped that this study will bring about new possibilities to the research in acoustic metasurfaces, especially in miniaturized acoustic devices. Such a metasurface based design and their realization through ~~new~~ additive manufacturing techniques, can hence be readily scaled down to operate at much higher frequencies, to find applications as compact acoustic devices for sensing, levitation, non-contact ultrasonic imaging and therapeutic ultrasound.

[1] B. Assouar, B. Liang, Y. Wu, Y. Li, J. C. Cheng, and Y. Jing, Nature Reviews Materials **3** (2018), 10.1038/s41578-018-0061-4.

[2] H. Ge, M. Yang, C. Ma, M. H. Lu, Y. F. Chen, N. Fang, and P. Sheng, National Science Review **5**, 159 (2018).

[3] S. A. Cummer, J. Christensen, and A. Alù, Nature Reviews Materials **1** (2016), 10.1038/natrevmats.2016.1.

[4] Y. Zhu, X. Fan, B. Liang, J. Cheng, and Y. Jing, Physical Review X **7**, 1 (2017).

[5] C. Shen, J. Xu, N. X. Fang, and Y. Jing, Physical Review X **4**, 1 (2014).

[6] G. Memoli, M. Caleap, M. Asakawa, D. R. Sahoo, B. W. Drinkwater, and S. Subramanian, Nature Communications **8**, Article 14608 (2017).

[7] Y. Li, C. Shen, Y. Xie, J. Li, W. Wang, S. A. Cummer, and Y. Jing, Physical Review Letters **119**, 035501 (2017).

[8] J. Li, C. Shen, A. Díaz-Rubio, S. A. Tretyakov, and S. A. Cummer, Nature Communications **9**, 1 (2018).

[9] Y. Xie, W. Wang, H. Chen, A. Konneker, B. I. Popa, and S. A. Cummer, Nature Communications **5**, 1 (2014).

[10] W. Wang, Y. Xie, B. I. Popa, and S. A. Cummer, Journal of Applied Physics **120** (2016), 10.1063/1.4967738.

[11] Y. Li, S. Qi, and M. B. Assouar, New Journal of Physics **18** (2016), 10.1088/1367-2630/18/4/043024.

[12] Y. Li, X. Jiang, B. Liang, J. C. Cheng, and L. Zhang, Physical Review Applied **4**, 1 (2015).

[13] Y. Xie, A. Konneker, B. I. Popa, and S. A. Cummer, Applied Physics Letters **103**, 1 (2013).

[14] Y. Li, B. Liang, X. Tao, X. F. Zhu, X. Y. Zou, and J. C. Cheng, Applied Physics Letters **101** (2012), 10.1063/1.4769984.

[15] K. Song, J. Kim, S. Hur, J.-H. Kwak, S.-H. Lee, and T. Kim, Scientific Reports **6**, 32300 (2016).

[16] C. Shen, A. Díaz-Rubio, J. Li, and S. A. Cummer, Applied Physics Letters **112** (2018), 10.1063/1.5025481.

[17] G. Y. Song, Q. Cheng, T. J. Cui, and Y. Jing, Physical Review Materials **2**, 065201 (2018).

[18] Y. Jing and S. A. Cummer, Scientific reports , 1 (2016).

[19] D. C. Skigin, M. Lester, S. Collin, M. Molerón, M. Serra-garcia, and C. Daraio, New Journal of Physics (2016), 10.1088/1367-2630/18/3/033003.

[20] X. Jiang, Y. Li, and L. Zhang, The Journal of the Acoustical Society of America **141**, EL363 (2017).

[21]N. J. Gerard, Y. Li, and Y. Jing, Journal of Applied Physics **123** (2018), 10.1063/1.5007863.

[22]F. Ju, Y. Tian, Y. Cheng, and X. Liu, Applied Physics Letters **113** (2018), 10.1063/1.5032263.

[23]C. Shen and S. A. Cummer, Physical Review Applied **9**, 54009 (2018).

[24]L. Zigoneanu, B. I. Popa, and S. A. Cummer, Physical Review B - Condensed Matter and Materials Physics **84**, 1 (2011).

[25]B. Liu, J. Zhao, X. Xu, W. Zhao, and Y. Jiang, Scientific Reports **7**, 1 (2017).

[26]Y. Xie, Y. Fu, Z. Jia, J. Li, C. Shen, Y. Xu, H. Chen, and S. A. Cummer, Scientific Reports **8**, 1 (2018).

[27]A. Marzo, S. A. Seah, B. W. Drinkwater, D. R. Sahoo, B. Long, and S. Subramanian, Nature Communications **6**, 1 (2015).

[28]G. T. Clement, H. Nomura, H. Adachi, and T. Kamakura, Physics in Medicine and Biology **58**, 6263 (2013).

[29]X. Zheng, W. Smith, J. Jackson, B. Moran, H. Cui, D. Chen, J. Ye, N. Fang, N. Rodriguez, T. Weisgraber, and C. M. Spadaccini, Nature Materials **15**, 1100 (2016).

[30]E. a. R. Ch, X. Y. Zheng, H. Lee, T. H. Weisgraber, M. Shusteff, J. DeOtte, E. B. Duoss, J. D. Kuntz, M. M. Biener, Q. Ge, J. A. Jackson, S. O. Kucheyev, N. X. Fang, and C. M. Spadaccini, Science **344**, 1373 (2014).

[31]C. Shen, Y. Xie, J. Li, S. A. Cummer, and Y. Jing, Applied Physics Letters **108**, 2 (2016).

[32]N. Yu, P. Genevet, M. a. Kats, F. Aieta, J.-P. Tetienne, F. Capasso, and Z. Gaburro, Science **334**, 333 (2011).

[33]Y. Li, B. Liang, Z.-m. Gu, X.-y. Zou, and J.-c. Cheng, Scientific reports **3**, 2546 (2013).

[34]J. Qian, J.-p. Xia, H.-x. Sun, S.-q. Yuan, Y. Ge, and X.-z. Yu, Journal of Applied Physics **122**, 244501 (2017).

[35]C. Shen, Y. Xie, J. Li, S. A. Cummer, and Y. Jing, Journal of Applied Physics **123** (2018), 10.1063/1.5009441.

[36]T. Liu, S. Liang, F. Chen, and J. Zhu, Journal of Applied Physics **123** (2018), 10.1063/1.4997631.

[37]Y. Zhu, J. Hu, X. Fan, J. Yang, B. Liang, X. Zhu, and J. Cheng, Nature Communications **9**, 1 (2018).

[38]Z. Tian, C. Shen, J. Li, E. Reit, Y. Gu, H. Fu, S. A. Cummer, and T. J. Huang, Advanced Functional Materials **1808489**, 1808489 (2019).